Response of convectively coupled Kelvin waves to surface temperature forcing in aquaplanet simulations

Mu-Ting Chien[1] and Daehyun Kim[1,2] *

[1]Department of Atmospheric Sciences, University of Washington

[2]School of Earth and Environmental Sciences, Seoul National University, South Korea

*Corresponding author: Daehyun Kim (daehyun@snu.ac.kr)

Key Points:

- Convectively coupled Kelvin waves (KWs) weaken and accelerate as the surface warms.
- Internal thermodynamic feedback is the dominant KW maintenance mechanism in our simulations.
- The weakening and acceleration of KWs with warming are associated with KWs transitioning from the second mode dynamics in -4K to the first mode dynamics in +4K.

Abstract

This study investigates changes in the propagation and maintenance of convectively coupled Kelvin waves (KWs) in response to surface warming. We use a set of three aquaplanet simulations made with the Community Atmospheric Model version 6 by varying the sea surface temperature boundary conditions, representing the current climate, a warmer (+4K), and a cooler (-4K) climate. Results show that KWs accelerate at the rate of about 7.1%/K and their amplitudes decrease by 4.7%/K. The dampening of KWs with warming is found to be associated with a weakening of the internal thermodynamic feedback between diabatic heating and temperature anomalies that generates KW eddy available potential energy (EAPE). The phase speed of KWs closely matches that of the second baroclinic mode KW in -4K, while the phase speed of KWs is approximately that of the first baroclinic mode KW in +4K. Meanwhile, the coupling between the two baroclinic modes weakens with warming. We hypothesize that in -4K, as the first and second modes are strongly coupled, KWs destabilize by positive EAPE generation within the second mode, and they propagate slower following the second mode KW phase speed. In +4K, as the first and second modes decouple, KWs are damped by negative EAPE generation within the first mode, and they propagate faster following the first mode KW phase speed.

Plain Language Summary

Convectively coupled Kelvin waves (KWs) regulate the variability of tropical precipitation on the subseasonal timescale. The change of KWs with surface warming is studied using three ocean-only global simulations with different sea surface temperatures. We find that KWs are weaker, and they propagate faster in a warmer climate. The results further suggest that the changes in the amplitude and phase speed of KWs with warming can be explained by the those in the thermodynamic structure of KWs.

1 Introduction

Convectively coupled Kelvin waves (KWs) are a dominant force in tropical subseasonal precipitation variability (Murata et al. 2006; Wang and Fu 2007; Sinclaire et al. 2015; Chen et al. 2019; Latos et al. 2021). These waves exert significant influence on global weather extremes and climate variability across multiple scales (Flatau et al. 2003; Bessafi and Wheeler 2006; Straub et al. 2006; Roundy 2008; Lawton and Majumdar 2023; Cheng et al. 2023). The profound impacts of KWs on such a broad spectrum of climatic phenomena underscore the necessity to understand their dynamics, particularly as the climate continues to warm.

While many studies have studied the changes in the Madden-Julian Oscillation (MJO) in a warmer climate (e.g., Adames et al. 2017a,b; Rushley et al. 2019; Bui and Maloney 2020), research into the response of convectively coupled equatorial waves (CCEWs) to similar conditions has been relatively scarce. Bartana et al. (2022) stands as an exception in this regard, utilizing global climate model (GCM) simulations from the sixth phase of the Coupled Model Intercomparison Project (CMIP6) to investigate CCEWs in a warming climate. Their findings indicate an intensification and acceleration of KWs with warming, as evidenced by increased KW variance in outgoing longwave radiation and upper tropospheric zonal wind, alongside an increase in the equivalent depth of the strongest KW signal strength. While they documented the changes in KW characteristics as the climate warms, however, the mechanisms behind the changes in KWs in a warmer climate remain unclear.

Previous observational and modeling studies have suggested two mechanisms for KW maintenance: the internal thermodynamic feedback and the external momentum forcing exerted by midlatitude Rossby waves. The internal feedback mechanism posits that KWs grow through the interaction between diabatic heating and temperature anomalies, which amplifies the KW eddy available potential energy (EAPE) (Lindzen 1974; Emanuel 1987; Mapes 2000; Straub and Kiladis 2003a; Khouider and Majda 2006; Raymond and Fuchs 2007; Kuang 2008; Chien and Kim 2023). While earlier simple models attributed this growth to deep convective clouds within the first baroclinic mode (e.g., Lindzen 1974; Emanuel 1987; Raymond and Fuchs 2007), more recent observational and modeling evidence highlighted the significant role of stratiform cloud processes within the second baroclinic mode (e.g., Mapes 2000; Straub and Kiladis 2003a; Khouider and Mada 2006; Kuang 2008; Chien and Kim 2023). Chien and Kim (2023), through a thorough analysis of KW EAPE growth rates in multiple reanalysis products, underscored the

dominance of the second baroclinic mode in the generation of KW EAPE. Their finding is consistent with the results of an earlier observational study which hypothesized that the presence of the second mode contributes to large KW EAPE generation in the upper troposphere (Straub and Kiladis 2003a).

In the meantime, studies have suggested that midlatitude Rossby waves, through a resonance mechanism involving momentum flux convergence in the subtropics and KW wind anomalies, could remotely amplify KW eddy kinetic energy (EKE) (Hoskins and Yang 2000; Straub and Kiladis 2003b; Tulich and Kiladis 2021; Cheng et al. 2022). When the midlatitude waves approach the critical latitude in the subtropics, which is the location where the background westerly wind has the same speed as the phase speed of the westward-propagating midlatitude waves, the wave propagation is blocked. This leads to the momentum flux convergence and divergence around the critical latitude, which acts as a transient forcing of the zonal wind (Randel and Held 1991). When the phase speed of such momentum forcing is the same as the phase speed of the KWs, the momentum forcing can resonate with KW zonal wind structures and thereby amplify the KWs. This remote influence of midlatitude waves is suggested to be important for KW maintenance in observations (Cheng et al. 2022) and aquaplanet simulations (Tulich and Kiladis 2021).

In a warmer climate, changes in the mean state may affect how convection and wave are coupled in the tropics, as well as the strength of midlatitude wave influence, which may change the relative importance of the internal and external mechanisms. In the present study, we investigate the relative importance of the two maintenance mechanisms across different climates to better understand changes in KW amplitude as the surface warms.

Regarding KW propagation, KWs propagate eastward at a speed of approximately 10-20 m/s in the current climate (Kiladis et al. 2009). This range of KW phase speeds is understood as the result of the dry Kelvin waves being slowed down due to the coupling with moist convection. Previous studies argued that the observed KW phase speed can be explained as either the first baroclinic mode dry Kelvin wave phase speed (~49 m/s) substantially reduced by convective coupling (e.g., Lindzen 1974; Emanuel 1987; Raymond and Fuchs 2007), or the second baroclinic mode dry Kelvin wave phase speed (~23 m/s) that is slightly reduced by convective coupling (e.g., Mapes 2000; Kuang 2008); debate persists over which offers a more accurate explanation of the observed KW phase speed. In a warmer climate, while changes in the mean

state and convective coupling of KWs potentially affect KW propagation, the specific effects of individual factors on KW phase speed with warming are yet to be determined.

Aquaplanet simulations—conducted on a water-covered Earth with idealized, time-independent sea surface temperatures (SST)—serve as our investigative tool. These simulations offer a simplified yet potent setting to explore the maintenance and propagation mechanisms of KWs, free from the confounding factors of seasonality and regionality (Straub and Kiladis 2002; Roundy and Frank 2004; Yang et al. 2007; Dias and Pauluis 2011; Yasunaga 2011; Wang and Chen 2016). Aquaplanet simulations have been used to study the characteristics of CCEWs, including KWs, and their interactions with the basic states (e.g., Leroux et al. 2016; Tulich and Kiladis 2021; Rios-Berrios et al. 2023). For example, Leroux et al. (2016) found that warm pool favors the development of MJO-like variability. Specifically targeting the maintenance of KWs and MJO, Tulich and Kiladis (2021) tested the importance of midlatitude waves and the effect of basic state zonal wind.

In the current study, we conduct and analyze aquaplanet simulations to investigate the changes in KWs with surface warming. While doing so, we quantify the relative roles of the internal thermodynamic feedback and the external forcing in maintaining KWs. We also investigate factors affecting KW propagation changes in different climates. The subsequent sections of this manuscript are organized as follows: Section 2 describes the design of our aquaplanet simulations and the methodologies employed for calculating the generation of KW EAPE and EKE, as well as the theoretical KW phase speed. Section 3 examines the changes in KW characteristics with warming, including the relative importance of the internal and external mechanisms of KW maintenance and the KW propagation mechanisms. A hypothesis on why KW amplitude and phase speed change with warming is proposed in the end. Finally, Section 4 consolidates our conclusions and summarizes the main findings of our study.

2 Simulations and Methods

2.1 Aquaplanet Simulations

Our study utilizes the sixth version of the Community Atmosphere Model (CAM6) to conduct aquaplanet simulations. The simulations operate on a horizontal grid resolution of 1.9° latitude by 2.5° longitude, encompassing 32 vertical levels. A brief description of the model dynamics and parameterization schemes used in these simulations is provided in Table 1. We run

136 the model over a twelve-year period, allocating the initial two years to the spin-up phase—
137 allowing the model to reach an equilibrium state—and dedicating the remaining ten years to the
138 data analysis phase, during which we collect 3-hourly output. We verify that equilibrium was
139 reached after the two-year integration period (now shown).
140
141 **Table 1**. Model dynamics and parameterization schemes used in our simulations.

Model component	Reference
Dynamical core	Finite Volume (Lin 2004)
Radiation	Rapid Radiative Transfer Model (RTMG, Iacono et al. 2008)
Deep convection	Zhang and McFarlane (1995)
Boundary layer turbulence, shallow convection, and cloud macrophysics	Cloud Layers Unified by Binormals (CLUBB, Golaz et al. 2002; Bogenschutz et al. 2013)
Cloud microphysics	Advanced Two-Moment Prognostic Cloud Microphysics (MG2, Gettlelman and Morrison 2015)

142
143 To assess the influence of surface temperatures on KWs, we design three experiments
144 using prescribed sea surface temperature (SST) conditions that are zonally uniform and time-
145 invariant. Following the "Qobs" profile in Neale and Hoskins (2000), the meridional profile of
146 SST in the control simulation (CTL) is designed as follows:

$$SST(\phi) = \begin{cases} 27 \times \left[1 - \frac{1}{2} \times sin^2\left(\frac{\pi\phi}{120}\right) - \frac{1}{2} \times sin^4\left(\frac{\pi\phi}{120}\right)\right], & |\phi| \leq 60^\circ \\ 0, & otherwise \end{cases} \quad (1)$$

147 , where ϕ denotes latitude. The SST boundary conditions for the other two experiments, named
148 +4K and -4K, are set by uniformly increasing and decreasing the SST globally by 4K,
149 respectively, relative to the SST in the CTL experiment. The time-averaged zonal mean

temperature and circulation for each simulation are shown in Figure 1, and the time-averaged zonal mean precipitation and precipitable water are shown in Figure 2.

2.2 KW meridional projection

To derive the characteristics of KWs from our simulation data, we first isolate anomalies for each field variable by subtracting the slowly varying climatological mean state. This process involves removing both the time-averaged mean and any variabilities with a period longer than 10 days, using a low-pass filter. The choice of a 10-day threshold is justified by the temporal scale of KWs in our simulations, which are typically shorter than this period.

We then focus on the tropical region, specifically between 10°S and 10°N, to examine the anomalies of precipitation, zonal wind, diabatic heating rate, and temperature. These anomalies are then projected onto the meridional structure characteristic of KWs—marked by a maximum at the equator and an exponential decay with latitude. The precise mathematical representation of this meridional structure is expressed as follows:

$$X_P = \int_{-\phi_{max}}^{\phi_{max}} X' \times w(\phi) \times e^{-\left(\frac{\phi}{\phi 0}\right)^2} \, d\phi, \tag{2}$$

where X represents field variables from aquaplanet simulations, including precipitation, zonal wind (u), diabatic heating (Q), and temperature (T), prime ($'$) denotes anomalies, ϕ denotes latitude, ϕ_0 represents the meridional scale of KWs (9˚ as in Tulich and Kialdis 2021 and Cheng et al. 2022), ϕ_{max}=10˚, and the weighting function w is defined as

$$w(\phi) = \begin{cases} 1, & |\phi| \le 10^\circ \\ 0, & otherwise \end{cases}. \tag{3}$$

Note that in this paper, diabatic heating rate refers to temperature tendency due to moist processes. We confirm that the temperature tendency due to other processes (e.g., radiation) within KWs is negligible (only contributing 5% to the total temperature tendency) in our simulations.

In addition, to quantify the impact of midlatitude waves on KW zonal wind anomalies, we compute the zonal momentum flux convergence (F), which is instrumental in understanding the extent to which midlatitude dynamics contribute to the momentum budget of tropical Kelvin waves. F is defined by the following expression:

$$F = -(\frac{\partial u'u'}{\partial x} + \frac{\partial u'v'}{\partial y} + \frac{\partial u'\omega'}{\partial p}), \quad (4)$$

where v and ω represent meridional and vertical velocity in pressure coordinates, respectively. To isolate the momentum flux convergence attributable specifically to midlatitude Rossby waves and to exclude the influence of other tropical variabilities, we apply an extratropical filter to the zonal momentum flux convergence (F), following Tulich and Kiladis (2021) and Cheng et al. (2022):

$$F_P = \int_{-\phi_{max}}^{\phi_{max}} F' \times (1 - w(\phi)) \times e^{-\left(\frac{\phi}{\phi_0}\right)^2} \, d\phi, \quad (5)$$

where Fp represents the meridionally-projected zonal momentum flux convergence, ϕ and ϕ_0 are the same as those in Eq. (2), and $\phi_{max} = 45^{\circ}$. The extratropical filter, denoted as $(1 - w(\phi))$, effectively diminishes the signal of tropical variability in the momentum flux convergence.

2.3 Space-time spectral analysis

We conduct a space-time spectral analysis on the equatorially symmetric component of precipitation anomalies. The raw power spectrum is normalized by the background spectrum, defined as the smoothed average of the raw spectrum. The resulting normalized power spectrum, which has often been referred to as the signal strength, is depicted in Figure 3.

We recognize that the spatial and temporal scale and the phase speed of KWs may exhibit variation across different climatic conditions. Consequently, instead of adopting the fixed KW band as defined by Wheeler and Kiladis (1999), we formulate our criteria to delineate the KW band. Specifically, we establish the KW band separately for each simulation by two distinct criteria: firstly, a high coherence squared between precipitation and column-integrated moisture; and secondly, a high coherence squared between precipitation and column-integrated temperature. These coherence relationships are visualized in Figure S1. These criteria are motivated by the understanding that KW precipitation is modulated by interactions with both atmospheric moisture and temperature, as suggested by recent findings (Weber et al. 2021). We posit that our tailored definition of the KW band is better suited for exploring the behavior of KWs under various climate scenarios.

To extract a time series representative of KW convective activity, we employ Fourier space-time filtering on the meridionally projected precipitation anomalies. This filtering technique selectively retains wave components falling within the KW band, which are outlined by purple contours in Figure 3. Based on the lag regression of KW-filtered precipitation in Fig. 4, we estimate the average frequency, zonal wavenumber, and phase speed of KWs.

2.4. KW composite

Upon the derivation of the KW precipitation time series, we employ the compositing approach of Nakamura and Takayabu (2022) to analyze the dynamical and thermodynamic structure of KWs. Based on the value of the KW precipitation anomaly and its position relative to the nearest local minimum and maximum, the KW phase is defined within the range of -π to π for each time and grid point. The most convectively active phase (π/2) is assigned to the local maximum, while the most convectively inactive phase (-π/2) is assigned to the local minimum. As in Nakamura and Takayabu (2022), we use local maxima and minima that are greater and smaller than plus and minus one standard deviation ($\pm 1\sigma$) of the KW-filtered precipitation anomalies in the entire dataset for each simulation, respectively. After determining the grid points with the most enhanced or suppressed phase, the beginning and end of each KW event are determined as the time when the KW-filtered precipitation anomalies reach an adjacent local minimum, local maximum, or zero, whichever occurs closest to the peak. The phase for each snapshot during a KW event is defined as the arcsine value of precipitation anomalies normalized by the nearest peak value.

Subsequently, all projected fields (Xp and Fp in Section 2.2) are composited based on the KW phase, resulting in KW composite fields (X_{KW}) as a function of the KW phase. By design, the KW precipitation anomalies evolve sinusoidally (Fig. 5). The amplitude of a KW event is quantified by averaging the absolute values of KW precipitation anomalies at the most enhanced and the most suppressed phases within the event (Fig. 5).

2.5 Vertical mode decomposition

To delineate the contributions of the first and second baroclinic modes to the maintenance and propagation of KWs, we perform an empirical vertical mode decomposition analysis, as in Chien and Kim (2023). For Q and T, we derive the vertical modes through the

rotated EOF analysis of Q. The first two leading EOFs are rotated to ensure that their structures are physically consistent with our understanding of the first and second baroclinic modes. The rotation is done by applying a rotation matrix to the original EOFs:

$$\begin{bmatrix} EOF1\_rotated \\ EOF2\_rotated \end{bmatrix} = \begin{bmatrix} EOF1\_original \\ EOF2\_original \end{bmatrix} * \begin{bmatrix} cos\,\theta & -sin\,\theta \\ sin\,\theta & cos\,\theta \end{bmatrix}, \tag{7}$$

where θ is the rotation angle. The rotation angle is chosen to maximize the vertical integral of the rotated first EOF for each simulation, which enforces the first mode to have a single-signed vertical structure.

For dynamical consistency between Q and U, we obtain the vertical modes of U from that of Q. Specifically, we first divide the rotated EOFs of Q by the mean static stability at each level to obtain the corresponding vertical structure of vertical velocity in pressure coordinate (ω). Then, we differentiate the resulting vertical structure of ω with respect to pressure to obtain vertical modes of U. Note that we apply 10 passes of 1-2-1 filter to the vertical profiles of Q and U for their smoothness. The two vertical modes for Q and U are shown in Figs. 6, 7, and 8.

2.6 EAPE and EKE growth rates

To assess the role of internal thermodynamic feedback and external forcing on KW maintenance, we compute the growth rates of the eddy available potential energy (EAPE) and eddy kinetic energy (EKE) that are associated with the first and second baroclinic modes using KW composite fields (Fig. 9). The growth rate of EAPE indicates the strength of internal thermodynamic feedback, while the growth rate of EKE reflects that of external dynamic feedback. We calculate the growth rates based on updated methods originating from Chien and Kim (2023) and Tulich and Kiladis (2021).

The growth rate of EAPE, which is the rate of EAPE generation normalized by the total EAPE, is proportional to the covariance between diabatic heating rate and temperature anomalies:

$$\sigma_{EAPE_i} = \frac{\overline{Q_{i,KW} \times T_{i,KW}}}{0.5 \times \overline{T_{i,kw}}^2}, \qquad i = 1\ or\ 2, \tag{8}$$

where subscript KW represents the KW composite fields, subscript i represents the vertical mode number. Similarly, the growth rate of EKE, which is the rate of EKE generation normalized by

the total EKE, is calculated based on the covariance between momentum flux convergence and zonal wind anomalies:

$$\sigma_{EKE_i} = \frac{\overline{F_{\iota,KW} \times U_{\iota,KW}}}{0.5 \times \overline{U_{\iota,KW}}^2}, \qquad i = 1 \; or \; 2. \tag{9}$$

2.7. KW propagation speed

Given the structural similarity between KWs and dry Kelvin waves, previous studies postulated that KWs are essentially manifestations of dry Kelvin waves influenced by moist convection, through modifying the adiabatic cooling and heating rates associated with the KW vertical motions (e.g., Kiladis et al. 2009). The adiabatic cooling and heating rates depend on the following physical parameters: the effective static stability, the tropospheric depth, and the vertical mode. In short, KWs propagate faster with increased effective static stability, increased tropospheric depth, and decreased vertical mode.

In a continuously stratified atmosphere, the phase speed of KWs can be determined as follows:

$$Cp = \sqrt{gh}, \tag{10}$$

where g is the gravitational acceleration constant, and h is the equivalent depth. The equivalent depth is defined as:

$$h = \frac{N^2(1-\alpha)}{g\left(m^2 + \frac{1}{4Hs^2}\right)}, \tag{11}$$

where N represents dry static stability, α represents the reduction of dry static stability by diabatic heating, and m is the vertical wavenumber, defined as m =$2\pi i/Lz$, with Lz being the tropospheric depth. The tropospheric depth Lz is estimated from the KW vertical structure of temperature. i denotes the vertical mode number defined in Section 2.5, and Hs is the scale height.

We calculate the theoretical phase speed of the first and second mode KW in each simulation (Fig. 10) based on Eqs (10) and (11) with the following estimation of the parameters: N is obtained from static stability profile weighted by each EOF mode, representing the static

stability that each vertical mode feels. The reduction factor α is estimated from the regression slope between the first two principal components of Q and the principal components of adiabatic cooling (ω*S), where S represents the static stability in pressure coordinates. The principal components of ω*S are obtained by projecting ω*S onto vertical mode of Q.

3 Results

3.1 Changes in KW phase speed and amplitude

The time-averaged zonal mean circulation in our simulations shows robust Hadley circulation in the tropics and the subtropical jet stream (Fig. 1), mimicking the observed mean climate. As the surface warms, tropospheric temperature increases, and the Hadley circulation expands further to the upper troposphere. Meanwhile, the mean precipitable water and precipitation increases from -4K to +4K, especially in the tropics (Fig. 2).

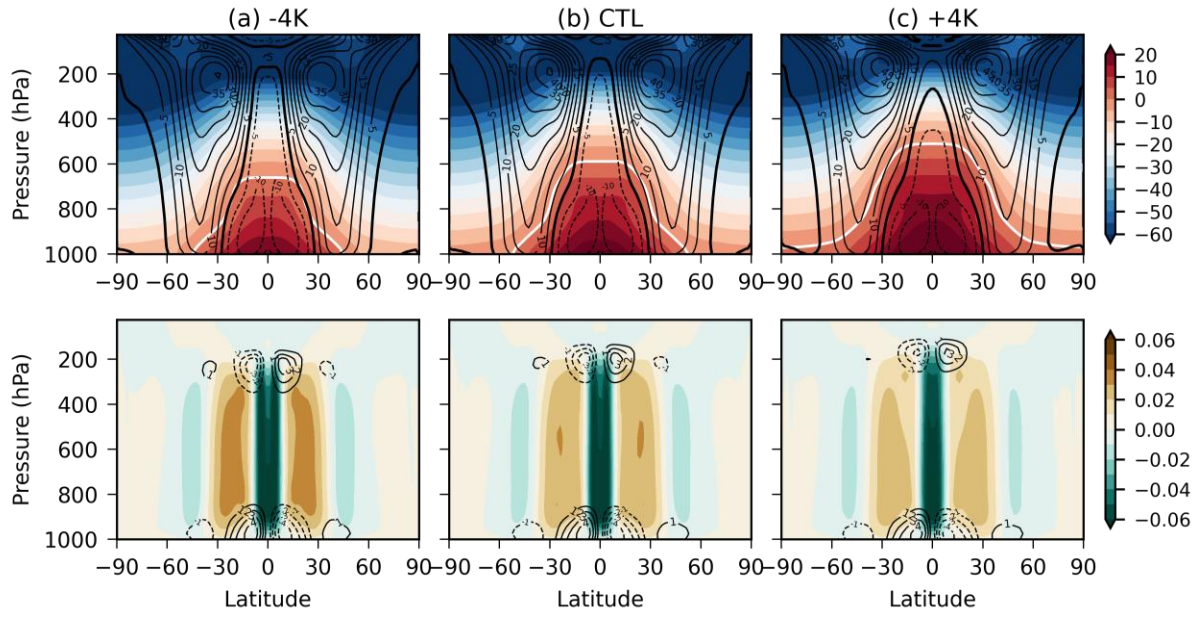

Figure 1. Time-averaged zonal mean circulation and temperature in each simulation. Figures on the top row show temperature (shading, ℃) and zonal wind (contours, m/s). The zero line for temperature (the melting level) is marked in white, and the zero line for zonal wind is marked in thick black line. Figures on the bottom row show vertical velocity (shading, Pa/s) and meridional velocity (contours, m/s).

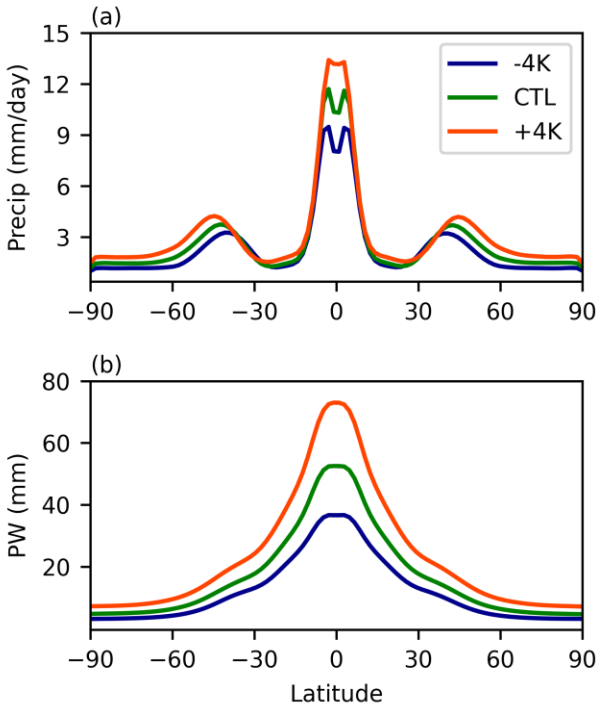

Figure 2. Time-averaged zonal mean (a) precipitation (mm/day) and (b) precipitable water (mm) in each simulation.

Despite the robust increase in the mean precipitation, different modes of subseasonal precipitation variabilities may respond differently to surface warming. To investigate the changes in subseasonal precipitation variabilities in wavenumber-frequency space, Figure 3 shows the normalized power spectrum of precipitation anomalies for the symmetric-to-the-equator component in -4K, CTL, and +4K simulations. As the surface warms, the low-frequency westward propagating signal (likely equatorial Rossby waves) weakens, and the low-frequency eastward propagating signal (likely MJO) strengthens. However, this is out of the scope of our paper as our focus is on KWs. KW bands are indicated in purple polygons with the boundaries in wavenumber-frequency space shown in Table 2. While KWs are pronounced in all simulations, the signal strength of precipitation within the KW band weakens from -4K to +4K. The raw power of precipitation within the KW band also weakens from -4K to +4K (not shown). In addition to the changes in KW amplitude, in a warmer climate, KWs appear in higher frequencies and align with the dispersive curve that corresponds to a higher equivalent depth, suggesting that KWs propagate faster.

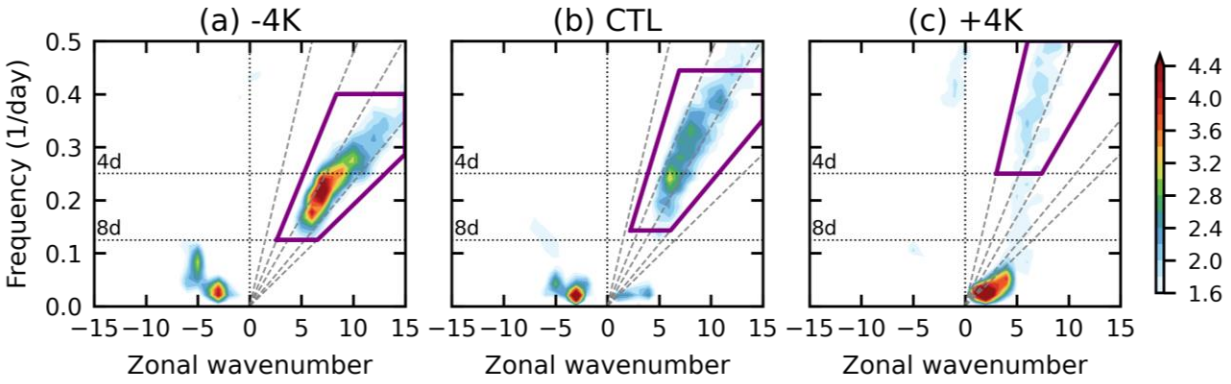

Figure 3. Normalized power spectrum of the equatorially symmetric component of precipitation anomalies over 15˚S-15˚N in each simulation. KW bands are indicated in purple polygons. The grey slanted dashed lines represent different equivalent depths, which are 8m, 12m, 25m, 50m, and 150m counterclockwise. The horizontal dotted lines indicate 4-day and 8-day.

Table 2. Boundaries of KW band in each simulation.

	-4K	CTL	+4K
Zonal wavenumber	1~15	1~15	1~15
Period (day)	2.5~8	2.25~7	2~4
Equivalent depth (m)	8~50	12~90	25~150

To better visualize the changes in KW characteristics, Figure 4 shows the lag regression of KW precipitation on the Hovmoller diagram, represented by the reference point at 180˚E. Note that the result is consistent regardless of any other longitudes chosen as reference points. Figure 4 shows that in a warmer climate, KWs are weaker and faster, and they appear in higher frequencies, consistent with the findings in Fig. 3. To quantify the changes in zonal wavenumber, frequency, and phase speed of KWs as the climate warms, we calculate the average zonal wavenumber, frequency, and phase speed for each simulation, as shown in Table 3. KW characteristics in Table 3 obtained from Figure 4 are consistent with the signal-strength-weighted average over the wavenumber-frequency space within the KW band based on Fig. 3 (not shown).

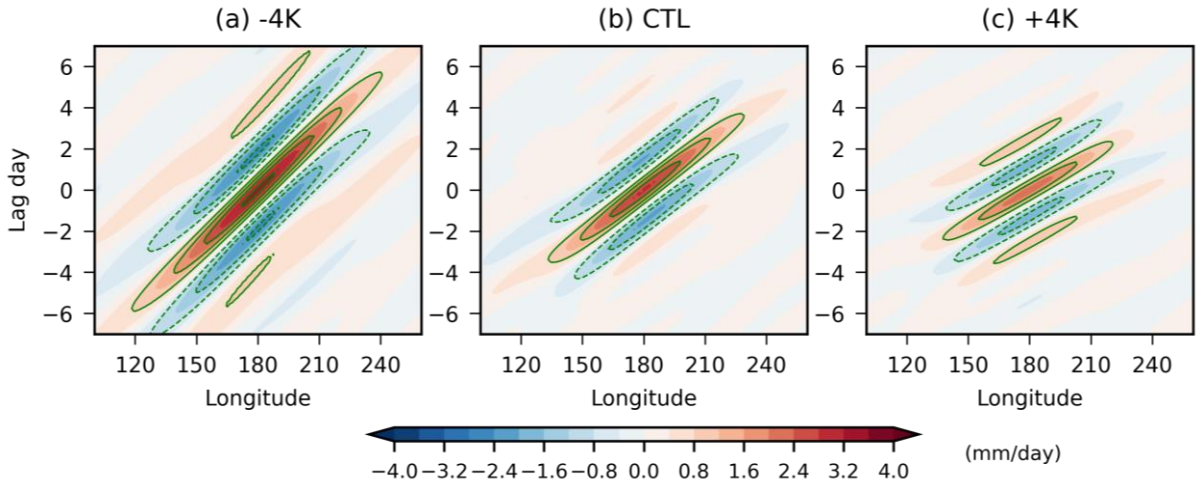

Figure 4. Lag regression of KW-filtered precipitation anomalies at each longitude upon those at the reference longitude (180˚E) in each simulation. The contour interval is 0.8 mm/day. Solid lines represent positive values and dashed lines represent negative values. Zero lines are omitted.

Table 3. KW characteristics in each simulation.

	-4K	CTL	+4K
Zonal wavenumber	9	9	8
Period (day)	3.75	3	2.5
Equivalent depth (m)	17.07	26.58	50.02
Phase speed (m/s)	12.94	16.14	22.14
Amplitude (mm/day)	3.26	2.85	2.19

Figure 5 shows the evolution of KW precipitation anomalies within the life cycle of KWs in each simulation. Note that the x-axis shows the KW phase, which can be considered as a time axis, with time increasing from the right to the left. Within the life cycle of KWs, precipitation anomalies present a sinusoidal evolution. Starting from the unperturbed phase (-π) when precipitation anomaly is zero, precipitation decreases until minimizing at the most suppressed phase (-π/2). Then, precipitation increases until maximizing at the most enhanced phase (π/2) and then returns to the unperturbed phase (π). While the sinusoidal evolution of precipitation anomalies exists in each simulation, KW amplitude decreases from 3.26 to 2.19 mm/day from -

4K to +4K (roughly -4.7%/K). In Section 3.2 and 3.3, we focus on investigating why KWs are weaker and faster in a warmer climate.

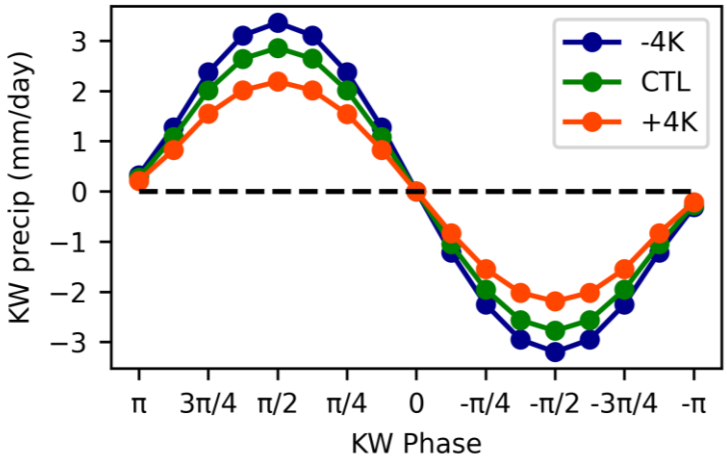

Figure 5. KW phase composite of precipitation anomalies in each simulation.

3.2. Causes of the changes in KW amplitude

To investigate the cause of the changes in KW phase speed and amplitude, analyzing the role of the first and second baroclinic modes is necessary, as mentioned in Section 1. Figure 6a displays the vertical structure of diabatic heating and temperature anomalies of the first and second baroclinic modes. Figure 6b shows the corresponding zonal wind and momentum flux convergence anomalies.

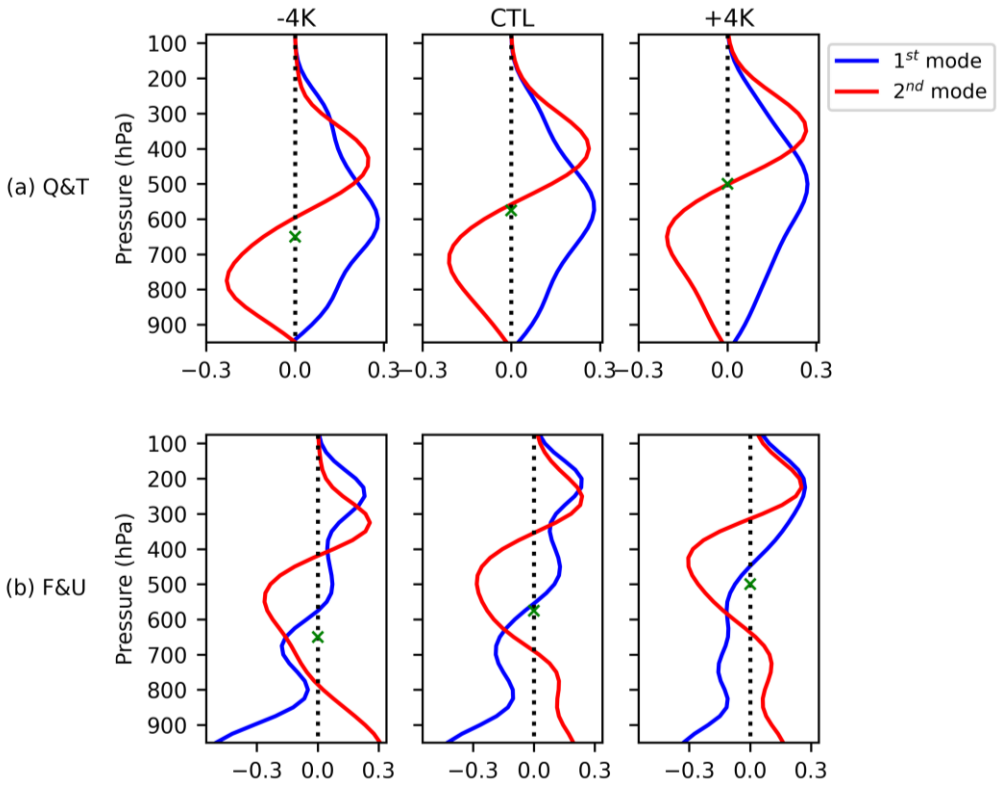

Figure 6. The vertical structure of the first (blue line) and second (red line) baroclinic modes of (a) diabatic heating and temperature, obtained from the EOF analysis of diabatic heating, and (b) zonal wind and momentum flux convergence, obtained from the vertical derivation of the EOF analysis of vertical pressure velocity in each simulation. Green crosses indicate the melting level, identified from the time-averaged zonal mean temperature profile in the tropics.

The two vertical modes in our simulations resemble the perceived structure of the first and second baroclinic modes. The first baroclinic structures represent the heating and circulation associated with deep convection. The first baroclinic heating structure presents a single signed heating over the entire tropics (blue lines in Fig. 6a) and the associated zonal wind structure exhibits opposite polarity between the upper and lower troposphere (blue lines in Fig. 6b). On the other hand, the second baroclinic structures represent the heating and circulation associated with stratiform and congestus processes. The second baroclinic heating structure is a dipole of heating and cooling (red lines in Fig. 6a), separated roughly by the melting level indicated with green crosses in Fig. 4a. The associated zonal wind structure (red lines in Fig. 6b) is characterized by three peaks in the upper-, mid-, and lower-troposphere.

From -4K to +4K, the structure of the first and second baroclinic modes expand further to the upper troposphere. The peak of the first baroclinic heating is shifted upward. Meanwhile, the most notable change in the second baroclinic heating structures is that the nodal point, which is

384 located close to the melting level (indicated in green crosses), is also shifted upward. Consistent
385 with the upward expansion of the heating structures, the zonal wind structures also expand
386 upward with warming.

387 To investigate the internal thermodynamic feedback in KW maintenance, Figure 7a shows
388 the KW composite vertical structure of diabatic heating (shading) and temperature (contour)
389 anomalies over the life cycle of KWs. In all simulations, negative heating anomalies peak when
390 precipitation is most suppressed (-π/2), and, as time goes on, heating anomalies increase and
391 maximize when precipitation anomalies are most enhanced (+π/2). From the most suppressed to
392 the most enhanced phase, temperature anomalies within KWs evolve from cold-aloft-warm-
393 below anomalies to warm-aloft-cold-below anomalies. The thermodynamic structure of KWs in
394 our simulations is consistent with that in observations, reanalyses, and other model simulations
395 (e.g., Kiladis et al. 2003; Tulich et al. 2007; Nakamura and Takayabu 2022; Chien and Kim
396 2023).

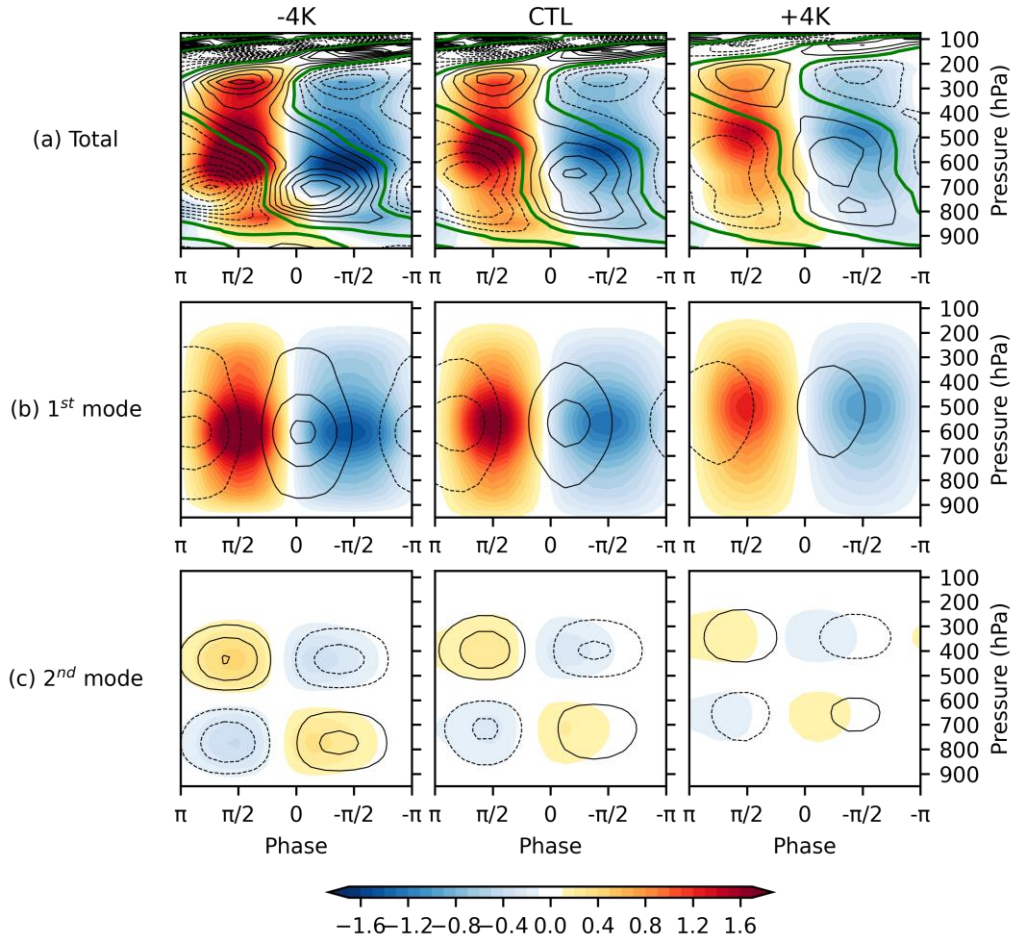

397

Figure 7. Vertical mode decomposition of the KW phase composite diabatic heating (shading) and temperature (contour) anomalies in each simulation: (a) the total anomalies, (b) the first baroclinic mode obtained from the blue lines in Fig. 6a, and (c) the second baroclinic mode obtained from the red lines in Fig. 6a. The green contour in (a) indicates the zero line for the temperature anomalies. Solid contours represent positive values and dashed contours represent negative values. The contour interval is 0.25 K.

Figure 7b shows the KW composite diabatic heating and temperature anomalies of the first baroclinic mode. The first mode heating minimizes at the most suppressed phase ($-\pi/2$) and maximizes at the most enhanced phase ($+\pi/2$), consistent with the evolution of precipitation anomalies. The temperature of the first mode is from in quadrature to slightly out of phase with the first mode heating anomalies, meaning that warm anomalies overlap with cooling and the cold anomalies overlap with heating, leading to a negative KW EAPE growth rate within the first mode (Fig. 9). Figure 7c shows the heating and temperature anomalies of the second baroclinic mode. The second mode heating anomalies with cooling aloft and heating below, indicating the congestus processes, occur slightly after the most suppressed phase; the second mode heating anomalies with heating aloft and cooling below, indicating the stratiform processes, slightly lag the deep convective heating by about $\pi/8$ to $\pi/4$. Opposite to the negative correlation between temperature and heating of the first mode, the second mode temperature anomalies are roughly in phase with the second mode heating and cooling, with warm anomalies overlapping with heating and cold anomalies overlapping with cooling. The positive correlation between temperature and heating of the second mode would lead to a positive KW EAPE growth rate within the second mode.

Figure 7b also shows that in a warmer climate, the first mode heating maximizes at a lower pressure level (higher elevation) (also shown in Fig. 4a), indicating deep convection deepens. Meanwhile, the out-of-phase relationship between the first mode heating and temperature is more obvious in a warmer climate, suggesting that the damping of the KW EAPE within the first mode structure is stronger. Figure 7c shows that in a warmer climate, the melting level rises, and the second mode structure stretches upward (also shown in Fig. 6a). Meanwhile, the lower tropospheric temperature anomalies near the boundary layer are weaker. In addition, from -4K to +4K, the second mode heating and temperature anomalies become less in phase, which suggests that the KW EAPE growth within the second mode decreases. As the surface

warms, the stronger KW EAPE damping of the first mode and the weaker KW EAPE growth may lead to the weakening of KWs.

To investigate the change in KW amplitude, we may also need to consider the effect of midlatitude forcing in KW maintenance. Figure 8a shows the KW composite vertical structure of momentum flux convergence (shading) and zonal wind (contour) anomalies. Figure 8b shows those of the first baroclinic mode. At the most suppressed phase ($-\pi/2$), the low-level zonal wind divergence and the upper-level zonal wind convergence are the strongest, consistent with the strongest first baroclinic cooling anomalies which are associated with the downward motion. Oppositely, at the most enhanced phase ($+\pi/2$), the low-level zonal wind convergence and the upper-level zonal wind divergence are the strongest, consistent with the strongest first baroclinic heating anomalies which are associated with the upward motion. Figure 8c shows the momentum flux convergence and zonal wind anomalies within the second baroclinic mode. The mid-level zonal wind divergence, which is the signature of the circulation associated with congestus clouds, occurs slightly after the most suppressed phase; the mid-level zonal wind convergence, which is the signature of the circulation of stratiform processes, occurs slightly after the most enhanced phase. The zonal wind structure in our simulations, as well as the thermodynamic structure in Fig. 7, show robust evolution from suppressed convection, congestus, deep convection, to stratiform processes within the life cycle of KWs, consistent with our understanding of canonical KWs.

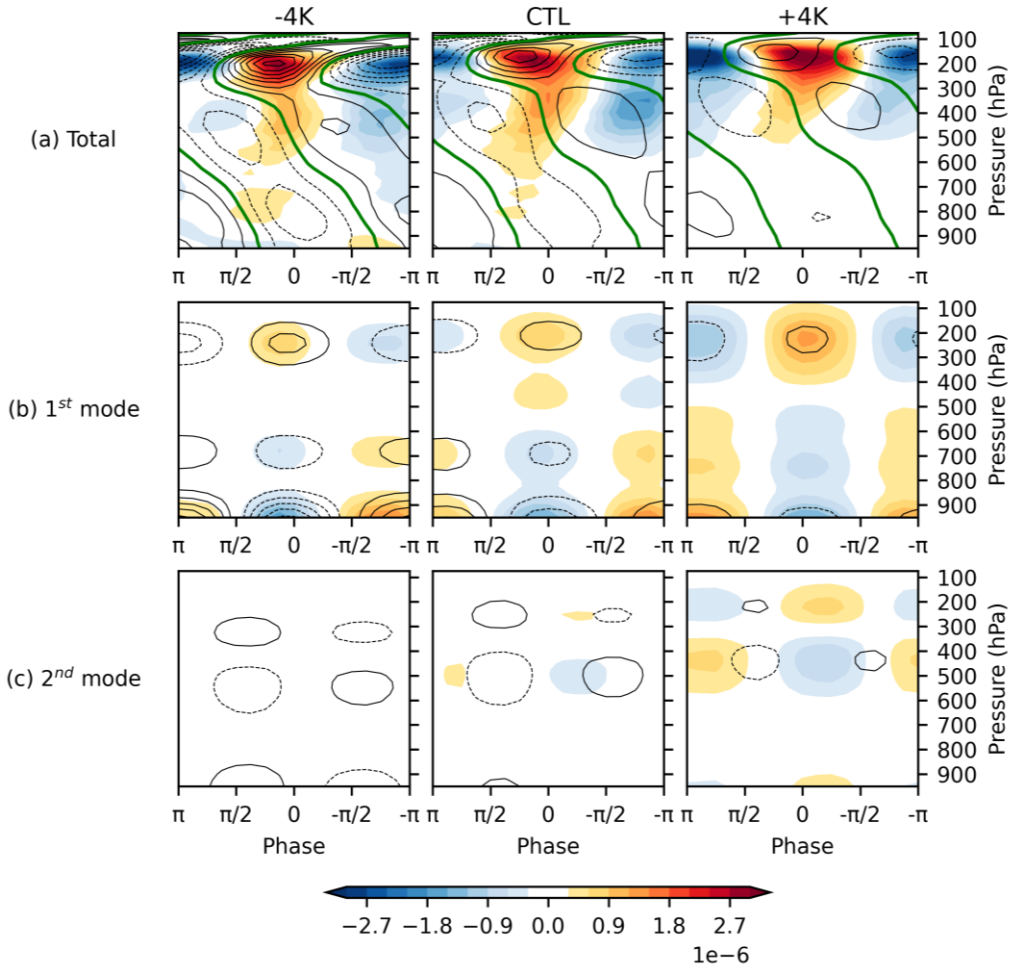

Figure 8. Vertical mode decomposition of the KW phase composite zonal momentum flux convergence (shading) and zonal wind anomalies (contour) in each simulation: (a) the total anomalies, (b) the first baroclinic mode obtained from the blue lines in Fig. 6b, and (c) the second baroclinic mode obtained from the red lines in Fig. 6b. The green contour in (a) indicates the zero line for the zonal wind anomalies. Solid contours represent positive values and dashed contours represent negative values. The contour interval is 2 m/s.

Figure 8a also shows that the momentum flux convergence maximizes at the upper levels near 200hPa, consistent with previous studies which showed that the extratropical influence on KWs originates from the upper troposphere (e.g., Straub and Kiladis 2003; Tulich and Kiladis 2021; Cheng et al. 2022). In all simulations, the upper-level momentum flux convergence coexists with the maximum KW westerly, while the momentum flux divergence coexists with the maximum KW easterly, which would amplify the KW EKE, as mentioned in Section 1. Similar to the vertical mode decomposition of diabatic heating and temperature anomalies in Fig. 7, the momentum flux convergence and zonal wind anomalies are also decomposed into the first

(Fig. 8b) and second (Fig. 8c) mode components. Figure 8b shows that the first mode zonal wind and momentum flux convergence positively overlap with each other, contributing to positive KW EKE growth rate of the first mode. Compared to the first mode, the second mode zonal wind and momentum flux convergence is less positively overlapping and more in quadrature (Fig. 8c), yielding a small KW EKE growth rate of the second mode.

From -4K to +4K, Figure 8b shows that the first mode zonal wind structure expands to the upper troposphere (also shown in Fig. 6b), consistent with the expansion of the depth of deep convection mentioned above (Fig. 7b). In terms of the magnitude changes from -4K to +4K, Figure 8b shows that the zonal wind anomalies weaken, and the momentum flux divergence anomalies strengthen. Stronger momentum flux divergence anomalies in a warmer climate may come from stronger midlatitude wave activities, or stronger midlatitude-tropics interactions due to the change in the basic state zonal wind, or both. In any case, our results suggest a larger KW EKE growth rate within the first mode, which may amplify KWs in a warmer climate. Stronger external forcing (Fig. 8) and weaker internal thermodynamic feedback (Fig. 7) in response to surface warming may amplify and weaken KWs, respectively. The amplitude change would depend on the relative magnitude of the KW EAPE and KW EKE growth rate.

To summarize the effect of internal thermodynamic feedback and external forcing on KW growth, Figure 9 shows the KW EAPE and KW EKE growth rates of the two vertical modes. In all simulations, the KW EKE growth rates, although positive, are roughly two orders of magnitudes smaller than that of the KW EAPE growth rates. This suggests that internal thermodynamic feedback is the dominant KW maintenance mechanism while the external momentum forcing only plays a minimal role in our simulations. Furthermore, the KW EAPE growth rate of the first mode (blue solid line) is negative and the KW EAPE growth rate of the second mode (red solid line) is positive in all simulations, consistent with what was shown in most reanalysis products (Chien and Kim 2023) and simple models which promote the importance of stratiform and congestus processes in KW destabilization (e.g., Mapes 2000; Khouider and Majda 2006; Kuang 2008).

From -4K to +4K, the KW EAPE growth of the second mode weakens while the KW EAPE damping of the first mode strengthens (shown in solid lines in Fig. 9, consistent with Fig. 7b-c). Meanwhile, the KW EKE growth of the first mode slightly strengthens with warming (shown in dashed lines in Fig. 9, consistent with Fig. 8b). To sum up, the weakening trend of

KW amplitude as the surface warms aligns with the decrease of KW EAPE growth of the first and second modes. This suggests that the weakening of KWs in a warmer climate is associated with the weakening of internal thermodynamic feedback, as opposed to the small increase of external forcing. However, it should be noted that the KW EAPE growth of the first or second mode alone cannot fully account for the weakening of KWs with surface warming.

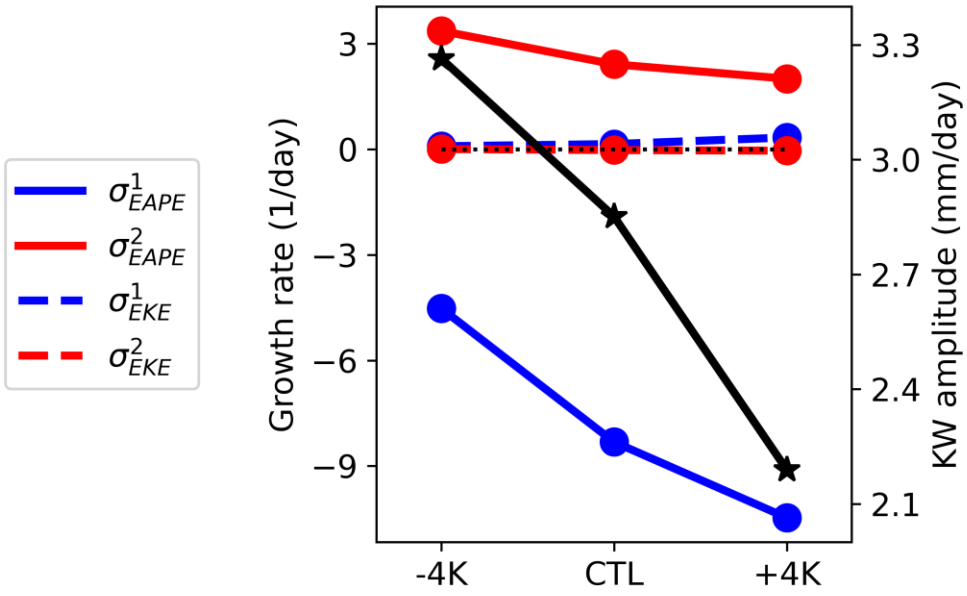

Figure 9. The growth rates of the KW EAPE (solid lines) and KW EKE (dashed lines) of the first and second modes in all simulations. The growth rates of the first mode are indicated in blue lines and those of the second mode are indicated in red lines. KW amplitude is indicated in black, with numbers showing on the y-axis on the right.

3.3. Causes of the changes in KW phase speed

Recall that we have shown that KWs accelerate with warming. To examine what factors determine the KW phase speed changes, we compare the apparent phase speed of KW convective signals with the theoretical phase speed of the two vertical modes (Fig. 10). While the apparent KW phase speed is estimated from the regression slope of KW precipitation in Fig. 4, the theoretical phase speeds of the two modes are calculated from Eqs. (10) and (11). The black line in Fig. 10a shows that the apparent KW phase speed increases from 12.94 m/s to 22.14 m/s from -4K to +4K (7.1 %/K). While KW phase speed may be affected by the mean barotropic zonal wind (Dias and Kiladis 2014), the increase in the mean barotropic zonal westerly by 2.9

m/s from -4K to +4K cannot fully explain the increase in KW phase speed by 9.2 m/s in our simulations. Therefore, the change in KW phase speed likely comes from the change in other factors (i.e. the terms in Eq. (11)). The theoretical KW phase speeds with the first or second baroclinic modes are shown in a blue and red line, respectively. The KWs with the first baroclinic structure propagate faster than the KWs with the second baroclinic structure. The phase speed of the KWs with the second baroclinic structure increases from 12.95 m/s to 15.03 m/s from -4K to +4K (1.9 %/K) and the phase speed of the KWs with the first baroclinic structure increases from 21.39 m/s to 24.03 m/s from -4K to CTL (3.1 %/K). The increase in the first or second mode KW phase speed with warming is mostly due to the increase in tropospheric depth (dashed lines in Fig. S2 b-c). The first mode KW phase speed slightly decreases from CTL to +4K, due to stronger offset of adiabatic cooling by diabatic heating (larger α in Eq. (11)) (dotted line in Fig. S2b), which overcomes the effect of increased tropospheric depth. Nevertheless, considering the changes in the KW phase speed of the first or second mode alone cannot fully account for the changes in the apparent KW phase speed. In fact, the apparent KW phase speed is closer to the second mode KW phase speed in -4K, whereas it is closer to the first mode KW phase speed in +4K.

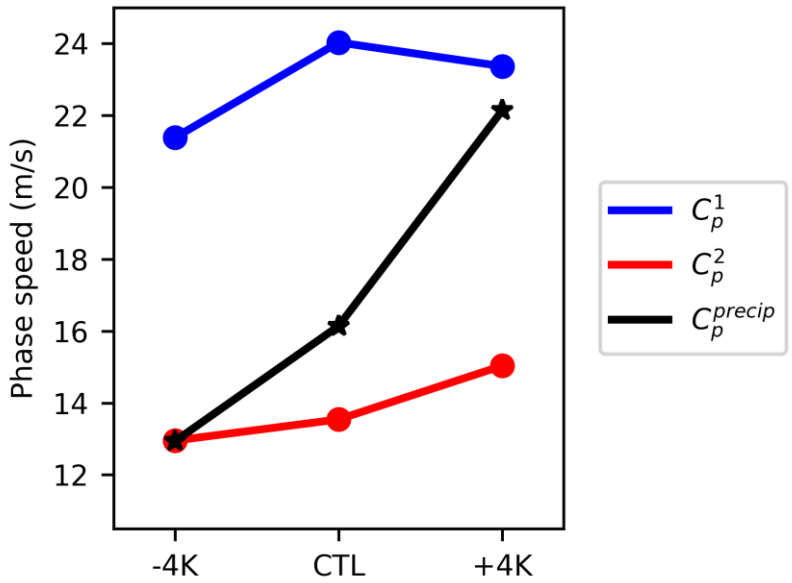

Figure 10. KW apparent phase speed (black, obtained from the regression slope in Fig. 4) and the theoretical KW phase speed for the first (blue) and second (red) modes (obtained from Eq. (10) and Eq. (11)) in all simulations.

3.4. Synthesis

Both the weakening and acceleration of KWs in response to surface warming cannot be solely explained by the changes in a single vertical mode, in terms of the KW EAPE growth (Fig. 9) or the estimated phase speed (Fig. 10). Specifically, KWs propagate slower at phase speed closer to that of the second mode KW in -4K, whereas in +4K, KWs propagate faster at phase speed closer to that of the first mode KW (Fig. 10). Meanwhile, stronger KWs in -4K may be due to the growth of the second mode via positive KW EAPE generation, while weaker KWs in +4K may be associated with the damping of the first mode via negative KW EAPE generation (Fig. 9). To investigate the coupling between the two modes, Figure 11 shows the coherence squared between the first and second mode heating in wavenumber-frequency space. Within the KW band, the first mode heating is strongly coupled with the second mode heating in -4K, while the two modes are weakly coupled in +4K.

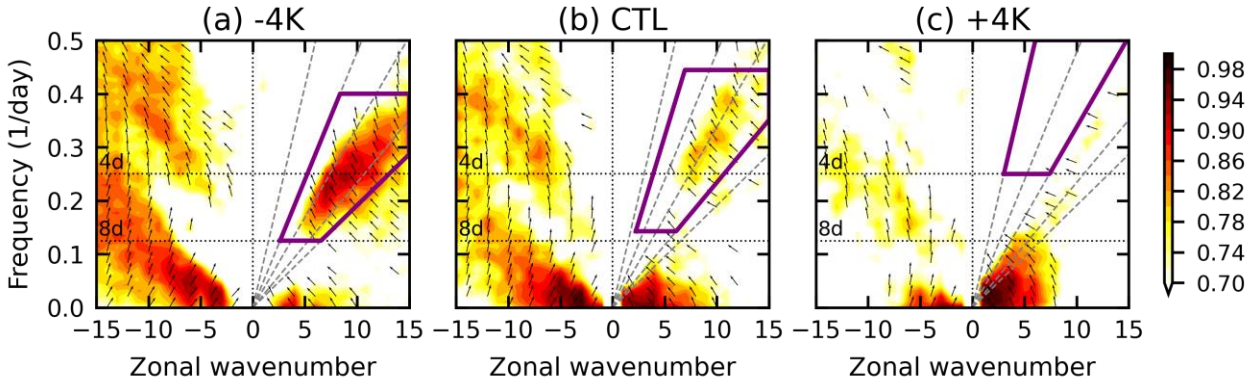

Figure 11. The coherence squared (shading) and phase relationship (arrows) between the first and second principal components of diabatic heating. Arrows pointing leftward (rightward) represent the second mode lagging (leading) the first mode; arrows pointing upward (downward) represent the second mode in phase (out of phase) with the first mode. KW band is indicated in purple polygons.

Synthesizing the results presented in Figs. 9, 10, and 11, we hypothesize that in -4K, when the first and second modes are strongly coupled, KWs destabilize through positive feedback between the second mode heating and temperature. This positive feedback would lead to stronger KWs (i.e., stronger temperature, zonal wind, and precipitation anomalies). Meanwhile, since KWs destabilize within the second mode component, their propagation speed also follows the second mode KW phase speed, which is determined by the adiabatic heating and cooling rate associated with the second baroclinic vertical motion. In +4K, as the first and second

567 modes are weakly coupled, KWs are less affected by the second modes, and thus they are
568 dominated by the first mode. The first mode heating is negatively correlated with the first mode
569 temperature variability, producing a negative KW EAPE growth rate. This negative feedback
570 would lead to weaker KWs (i.e., weaker temperature, zonal wind, and precipitation anomalies).
571 Meanwhile, since the first baroclinic mode dominates KWs, the propagation speed of the KWs is
572 faster, as it follows the first mode KW phase speed. This faster first mode phase speed is due to a
573 stronger adiabatic cooling and heating associated with the first baroclinic vertical motion than
574 those of the second baroclinic motion.

575 **4 Summary and Conclusions**

576 This study investigated the changes in KW characteristics in response to surface warming
577 and explored their causes. We conducted a set of three aquaplanet simulations by prescribing
578 zonally uniform and meridionally varying sea surface temperatures (SST) boundary conditions.
579 For the control simulation, a profile based on the observed SST distribution is used (Neale and
580 Hoskins 2000). For warmer and cooler climates, we added and subtracted 4K uniformly over the
581 entire globe (+4K and -4K, respectively). The simulation results showed that KWs weakened
582 and accelerated as the surface warms. The eddy available potential energy (EAPE) and eddy
583 kinetic energy (EKE) budget of the KWs suggested that KWs in the simulations were mainly
584 maintained by the internal thermodynamic feedback. We found that the weakening of KWs was
585 associated with (1) a weakening of positive EAPE generation within the second baroclinic mode
586 and (2) a strengthening of negative EAPE generation within the first baroclinic mode. In
587 addition, the KW phase speed diagnostics showed that KWs' phase speed in -4K (~12.94 m/s) is
588 close to the theoretical second mode KW phase speed, while their phase speed in +4K (~22.14
589 m/s) is close to the theoretical first mode KW phase speed. We also found that the first and
590 second modes were strongly coupled within KWs in -4K, while they are weakly coupled in +4K.
591 Synthesizing our results, we hypothesized that the KWs weakened and accelerated with
592 warming because different dynamics dominated KWs' propagation and maintenance. In -4K,
593 KWs destabilize through positive feedback between the second mode heating and temperature,
594 which is possible because the first and second baroclinic modes are strongly coupled. This
595 positive feedback would lead to stronger KWs (i.e., stronger temperature, zonal wind, and
596 precipitation anomalies). Meanwhile, since KWs destabilize within the second mode component,

their propagation speed follows the theoretical second mode KW phase speed. In +4K, as the coupling between the first and second modes weakens, KWs dynamics appear to be dominated by that of the first baroclinic mode KWs. Because the first mode heating is negatively correlated with the first mode temperature variability, producing a negative EAPE growth rate, KWs in +4K are damped and hence exhibit weaker variability (i.e., weaker temperature, zonal wind, and precipitation anomalies). Meanwhile, since the first baroclinic mode dynamics dominates, the propagation speed of KWs follows that of the theoretical first mode KW phase speed.

Our results suggest that the mean state changes have substantial impacts on the amplitude and phase speed of KWs. One of the remaining important questions is why the coupling between the two vertical modes weakens in a warmer climate. An in-depth study of the coupling mechanism is warranted, which should also examine whether our simulation results can be explained by any of the previously proposed coupling mechanisms (e.g., Mapes 2000; Khouider and Majda 2006; Kuang 2008).

It is worth noting that our results contradict to that of Bartana et al. (2022), who found that KWs intensify in a warmer climate in CMIP6 models. A possible reason for the discrepancy is the difference in the mean state temperature changes. While we use zonally uniform and meridionally symmetric SST profiles, the SST changes in CMIP6 model simulations have strong zonal and meridional asymmetry. To what extent the SST asymmetry affects the changes of KWs is not clear. Future studies can use more realistic SST warming and cooling patterns to investigate the extent to which zonal and meridional asymmetry of SST changes affect KW characteristics.

Acknowledgments

The aquaplanet simulations were performed based on high-performance computing resources from Cheyenne (doi:10.5065/D6RX99HX) and Derecho (doi: 10.5065/qx9a-pg09) provided by NCAR's Computational and Information Systems Laboratory, sponsored by the National Science Foundation. MC was supported by PhD Fellowship from Taiwanese Ministry of Science and Technology. DK was supported by New Faculty Startup Fund from Seoul National University, NASA MAP program (80NSSC21K1495), NOAA MAPP program (NA21OAR4310343), and NOAA CVP program (NA22OAR4310608).

Open Research

The aquaplanet simulation outputs and the codes for analysis are uploaded on Github with the following link: https://github.com/muting-chien/CCKW_aquaplanet. The analysis codes are written mostly in functions, and therefore they can be easily applied to analyze KWs in observations and other model simulations.

References

Adames, Á. F., D. Kim, A. H. Sobel, A. Del Genio, and J. Wu, 2017a: Changes in the structure and propagation of the MJO with increasing CO2. *J. Adv. Model. Earth Syst.*, 9, 1251–1268, https://doi.org/10.1002/2017MS000913

Adames, Á. F., D. Kim, A. H. Sobel, A. Del Genio, and J. Wu, 2017b: Characterization of Moist Processes Associated With Changes in the Propagation of the MJO With Increasing CO 2. J. Adv. Model. Earth Syst., 9, 2946–2967, https://doi.org/10.1002/2017MS001040

Bartana, H., Garfinkel, C. I., Shamir, O., & Rao, J. (2022). Projected future changes in equatorial wave spectrum in CMIP6. *Climate Dynamics*, 1-13, https://doi.org/10.1007/s00382-022-06510-y

Bessafi, M., and M. C. Wheeler, 2006: Modulation of south Indian Ocean tropical cyclones by the Madden–Julian oscillation and convectively coupled equatorial waves. *Mon. Wea. Rev.*, 134, 638–656, https://doi.org/10.1175/MWR3087.1.

Bogenschutz, P. A., Gettelman, A., Morrison, H., Larson, V. E., Craig, C., & Schanen, D. P. (2013). Higher-order turbulence closure and its impact on climate simulations in the Community Atmosphere Model. *Journal of Climate*, *26*(23), 9655-9676, https://doi.org/10.1175/JCLI-D-13-00075.1

Bui, H. X., and E. D. Maloney, 2020: Changes to the Madden-Julian Oscillation in Coupled and Uncoupled Aquaplanet Simulations With 4xCO2. *J. Adv. Model. Earth Syst.*, 12, e2020MS0021799, https://doi.org/10.1029/2020MS002179

Chen, W. T., Hsu, S. P., Tsai, Y. H., & Sui, C. H. (2019). The influences of convectively coupled Kelvin waves on multiscale rainfall variability over the South China Sea and Maritime Continent in December 2016. *Journal of Climate*, 32(20), 6977-6993, https://doi.org/10.1175/JCLI-D-18-0471.1

Cheng, Y. M., Tulich, S., Kiladis, G. N., & Dias, J. (2022). Two extratropical pathways to forcing tropical convective disturbances. *Journal of Climate*, *35*(20), 2987-3009, https://doi.org/10.1175/JCLI-D-22-0171.1

Cheng, Y. M., Dias, J., Kiladis, G., Feng, Z., & Leung, L. R. (2023). Mesoscale convective systems modulated by convectively coupled equatorial waves. *Geophysical Research Letters*, *50*(10), e2023GL103335. https://doi.org/10.1029/2023GL103335

Chien, M. T., & Kim, D. (2023). Representation of the Convectively Coupled Kelvin Waves in Modern Reanalysis Products. *Journal of the Atmospheric Sciences*, *80*(2), 397-418, https://doi.org/10.1175/JAS-D-22-0067.1

Computational and Information Systems Laboratory. (2019). Cheyenne: HPE/SGI ICE XA System (University Community Computing). Boulder, CO: National Center for Atmospheric Research. https://doi.org/10.5065/D6RX99HX.

Computational and Information Systems Laboratory. (2024). Derecho: HPE Cray EX System (University Community Computing). Boulder, CO: National Center for Atmospheric Research. https://doi.org/10.5065/qx9a-pg09.

Dias, J., & Pauluis, O. (2011). Modulations of the phase speed of convectively coupled Kelvin waves by the ITCZ. *Journal of the atmospheric sciences*, *68*(7), 1446-1459, https://doi.org/10.1175/2011JAS3630.1

689 Dias, J., & Kiladis, G. N. (2014). Influence of the basic state zonal flow on convectively coupled
690 equatorial waves. *Geophysical Research Letters*, *41*(19), 6904-6913,
691 https://doi.org/10.1002/2014GL061476
692
693 Emanuel, K. A., 1987: An air–sea interaction model of intraseasonal oscillations in the tropics. *J.*
694 *Atmos. Sci.*, 44, 2324–2340, https://doi.org/10.1175/1520-
695 0469(1987)044,2324:AASIMO.2.0.CO;2.
696
697 Flatau, M. K., P. J. Flatau, J. Schmidt, and G. N. Kiladis, 2003: Delayed onset of the 2002 Indian
698 monsoon. Geophys. Res. Lett., 30, 1768, https://doi.org/10.1029/2003GL017434.
699
700 Gettelman, A., & Morrison, H. (2015). Advanced two-moment bulk microphysics for global
701 models. Part I: Off-line tests and comparison with other schemes. *Journal of Climate*, *28*(3),
702 1268-1287, https://doi.org/10.1175/JCLI-D-14-00102.1
703
704
705 Golaz, J. C., Larson, V. E., & Cotton, W. R. (2002). A PDF-based model for boundary layer
706 clouds. Part I: Method and model description. *Journal of the atmospheric sciences*, *59*(24), 3540-
707 3551, https://doi.org/10.1175/1520-0469(2002)059<3540:APBMFB>2.0.CO;2
708
709 Hoskins, B. J., & Yang, G. Y. (2000). The equatorial response to higher-latitude forcing. *Journal*
710 *of the atmospheric sciences*, *57*(9), 1197-1213, https://doi.org/10.1175/1520-
711 0469(2000)057<1197:TERTHL>2.0.CO;2
712
713 Iacono, M. J., Delamere, J. S., Mlawer, E. J., Shephard, M. W., Clough, S. A., & Collins, W. D.
714 (2008). Radiative forcing by long-lived greenhouse gases: Calculations with the AER radiative
715 transfer models. *Journal of Geophysical Research: Atmospheres*, *113*(D13),
716 https://doi.org/10.1029/2008JD009944
717

718 Kiladis, G. N., Wheeler, M. C., Haertel, P. T., Straub, K. H., & Roundy, P. E. (2009).
719 Convectively coupled equatorial waves. *Reviews of Geophysics*, *47*(2),
720 https://doi.org/10.1029/2008RG000266
721
722 Khouider, B., & Majda, A. J. (2006). A simple multicloud parameterization for convectively
723 coupled tropical waves. Part I: Linear analysis. *Journal of the atmospheric sciences*, *63*(4), 1308-
724 1323, https://doi.org/10.1175/JAS3677.1
725
726 Kuang, Z., 2008: A moisture-stratiform instability for convectively coupled waves. *J. Atmos.*
727 *Sci.*, 65, 834–854, https://doi.org/10.1175/2007JAS2444.1.
728
729 Lawton, Q. A., & Majumdar, S. J. (2023). Convectively Coupled Kelvin Waves and Tropical
730 Cyclogenesis: Connections through Convection and Moisture. *Monthly weather review*, *151*(7),
731 1647-1666, https://doi.org/10.1175/MWR-D-23-0005.1
732
733 Latos, B., and Coauthors, 2021: Equatorial waves triggering extreme rainfall and floods in
734 southwest Sulawesi, Indonesia. *Mon. Wea. Rev.*, 149, 1381–1401,
735 https://doi.org/10.1175/MWRD-20-0262.1.
736
737 Leroux, S., Bellon, G., Roehrig, R., Caian, M., Klingaman, N. P., Lafore, J. P., ... & Tyteca, S.
738 (2016). Inter-model comparison of subseasonal tropical variability in aquaplanet experiments:
739 Effect of a warm pool. *Journal of Advances in Modeling Earth Systems*, *8*(4), 1526-1551,
740 https://doi.org/10.1002/2016MS000683
741
742 Lin, S. J. (2004). A "vertically Lagrangian" finite-volume dynamical core for global
743 models. *Monthly Weather Review*, *132*(10), 2293-2307, https://doi.org/10.1175/1520-
744 0493(2004)132<2293:AVLFDC>2.0.CO;2
745
746 Lindzen, R. S., 1974: Wave-CISK in the tropics. *J. Atmos. Sci.*, 31, 156–179,
747 https://doi.org/10.1175/1520-0469(1974)031,0156:WCITT.2.0.CO;2.
748

749 Mapes, B. E., 2000: Convective inhibition, subgrid-scale triggering energy, and stratiform
750 instability in a toy tropical wave model. *J. Atmos. Sci.*, 57, 1515–1535,
751 https://doi.org/10.1175/1520-469(2000)057,1515:CISSTE.2.0.CO;2.
752
753 Murata, F., M. D. Yamanaka, H. Hashiguchi, S. Mori, M. Kudsy, T. Sribimawati, B. Suhardi,
754 and Emrizal, 2006: Dry intrusions following eastward-propagating synoptic-scale cloud systems
755 over Sumatera Island. *J. Meteor. Soc. Japan*, 84, 277–294, https://doi.org/10.2151/jmsj.84.277.
756
757 Nakamura, Y., & Takayabu, Y. N. (2022). Convective Couplings with Equatorial Rossby Waves
758 and Equatorial Kelvin Waves. Part I: Coupled Wave Structures. *Journal of the Atmospheric*
759 *Sciences*, *79*(1), 247-262, https://doi.org/10.1175/JAS-D-21-0080.1
760
761 Neale, R. B., & Hoskins, B. J. (2000). A standard test for AGCMs including their physical
762 parametrizations: I: The proposal. *Atmospheric Science Letters*, *1*(2), 101-107,
763 https://doi.org/10.1006/asle.2000.0019
764
765 Randel, W., & Held, I. (1991). Phase speed spectra of transient eddy fluxes and critical layer
766 absorption. *Journal of the atmospheric sciences*, *48*(5), 688-697, https://doi.org/10.1175/1520-
767 0469(1991)048<0688:PSSOTE>2.0.CO;2
768
769 Raymond, D. J., and Zˇ . Fuchs, 2007: Convectively coupled gravity and moisture modes in a
770 simple atmospheric model. *Tellus*, 59A, 627–640, https://doi.org/10.1111/j.1600-
771 0870.2007.00268.x.
772
773 Rios-Berrios, R., Judt, F., Bryan, G., Medeiros, B., & Wang, W. (2023). Three-Dimensional
774 Structure of Convectively Coupled Equatorial Waves in Aquaplanet Experiments with Resolved
775 or Parameterized Convection. *Journal of Climate*, 1-44, https://doi.org/10.1175/JCLI-D-22-
776 0422.1
777
778 Roundy, P. E., 2008: Analysis of convectively coupled Kelvin waves in the Indian Ocean MJO.
779 *J. Atmos. Sci.*, 65, 1342–1359, https://doi.org/10.1175/2007JAS2345.1.

Roundy, P. E. and W. M. Frank, 2004: A climatology of waves in the equatorial region. *J. Atmos. Sci.*, 61, 2105–2132, https://doi.org/10.1175/1520-0469(2004)061,2105:ACOWIT.2.0.CO;2.

Rushley, S. S., Kim, D., & Adames, Á. F. (2019). Changes in the MJO under greenhouse gas–induced warming in CMIP5 models. *Journal of Climate*, *32*(3), 803-821, https://doi.org/10.1175/JCLI-D-18-0437.1

Sinclaire, Z., A. Lenouo, C. Tchawoua, and S. Janicot, 2015: Synoptic Kelvin type perturbation waves over Congo basin over the period 1979–2010. *J. Atmos. Sol.-Terr. Phys.*, 130–131, 43–56, https://doi.org/10.1016/j.jastp.2015.04.015.

Straub, K. H., and G. N. Kiladis, 2002: Observations of a convectively coupled Kelvin wave in the eastern Pacific ITCZ. *J. Atmos. Sci.*, 59, 30–53, https://doi.org/10.1175/1520-0469(2002)059,0030:OOACCK.2.0.CO;2.

Straub, K. H, G. N. Kiladis, 2003a: The observed structure of convectively coupled Kelvin waves: Comparison with simple models of coupled wave instability. *J. Atmos. Sci.*, 60, 1655–1668, https://doi.org/10.1175/1520-0469(2003)060,1655:TOSOCC.2.0.CO;2.

Straub, K. H., & Kiladis, G. N, 2003b. Extratropical forcing of convectively coupled Kelvin waves during austral winter. *Journal of the atmospheric sciences*, *60*(3), 526-543, https://doi.org/10.1175/1520-0469(2003)060<0526:EFOCCK>2.0.CO;2

Straub, K. H., G. N. Kiladis, and P. E. Ciesielski, 2006: The role of equatorial waves in the onset of the South China Sea summer monsoon and the demise of El Ni ˜no during 1998. *Dyn. Atmos. Oceans*, 42, 216–238, https://doi.org/10.1016/j.dynatmoce.2006.02.005.

809 Tulich, S. N., & Kiladis, G. N. (2021). On the regionality of moist Kelvin waves and the MJO:
810 The critical role of the background zonal flow. *Journal of Advances in Modeling Earth Systems*,
811 *13*(9), e2021MS002528, https://doi.org/10.1029/2021MS002528
812
813 Wang, H., and R. Fu, 2007: The influence of Amazon rainfall on the Atlantic ITCZ through
814 convectively coupled Kelvin waves. *J. Climate*, 20, 1188–1201,
815 https://doi.org/10.1175/JCLI4061.1.
816
817 Wang, L., and L. Chen, 2016: Interannual variation of convectively coupled equatorial waves
818 and their association with environmental factors. *Dyn. Atmos. Oceans*, 76, 116–126,
819 https://doi.org/10.1016/j.dynatmoce.2016.10.004.
820
821 Weber, Nicholas J., Daehyun Kim, and Clifford F. Mass. "Convection–Kelvin wave coupling in
822 a global convection-permitting model." *Journal of the Atmospheric Sciences* 78.4 (2021): 1039-
823 1055, https://doi.org/10.1175/JAS-D-20-0243.1
824
825 Wheeler, M., and G. N. Kiladis, 1999: Convectively coupled equatorial waves: Analysis of
826 clouds and temperature in the wavenumber–frequency domain. *J. Atmos. Sci.*, 56, 374–399,
827 https://doi.org/10.1175/1520-0469(1999)056,0374:CCEWAO.2.0.CO;2.
828
829 Yang, G. Y., Hoskins, B., & Slingo, J. (2007). Convectively coupled equatorial waves. Part I:
830 Horizontal and vertical structures. *Journal of the atmospheric sciences*, *64*(10), 3406-3423,
831 https://doi.org/10.1175/JAS4017.1
832
833 Yasunaga, K., 2011: Seasonality and regionality of the Madden-Julian oscillation and
834 convectively coupled equatorial waves. *SOLA*, 7, 153–156, https://doi.org/10.2151/sola.2011-
835 039.
836
837 Zhang, G. J., & McFarlane, N. A. (1995). Role of convective scale momentum transport in
838 climate simulation. *Journal of Geophysical Research: Atmospheres*, *100*(D1), 1417-1426,
839 https://doi.org/10.1029/94JD02519